Article

Stabilizing the Lithium-Rich Manganese-Based Oxide Cathode via Regulating a CEI Film

Zhuoran Feng, Leyi Guo, Xiaofei Liu, Wenwen Li, Ruipeng Zhang, Dong Wang,* Wei Zhang,* and Weitao Zheng

Cite This: https://doi.org/10.1021/acsaem.3c03224

Read Online

ACCESS | Metrics & More | Article Recommendations | Supporting Information

ABSTRACT: Targeting high-energy-density batteries, lithium-rich manganese oxide (LMO), with its merits of high working voltage ($\sim$4.8 V vs Li/Li$^+$) and high capacity ($\sim$250 mAh g^{-1}), was considered a promising cathode for a 500 Wh kg^{-1} project. However, the practical application of LMO was hindered by the parasitic reaction between the electrolyte and the electrode, such as dissolution of surface lattice oxygen. Herein, N-methyl-N-trimethylsilyl trifluoroacetamide (MSTFA) is introduced as an additive in a common carbonate ester electrolyte to modify the cathode-electrolyte interphase (CEI) for blocking the undesirable side reaction. The preferential decomposition of MSTFA results in silicon and NO$_x$-containing CEI, which greatly enhances the high-voltage stability of the LMO cathode. Moreover, the designed CEI enables providing a homogeneous interphase within 5 nm, which is responsible for the long-time stability of the cathode. Herein, the assembled LMO∥Li battery yields a high-capacity retention of 93.1% after 200 cycles at a current density of 100 mA g^{-1}.

KEYWORDS: electrolyte additive, cathode-electrolyte interphase, high-voltage condition, lithium-rich manganese oxide, Li-ion battery
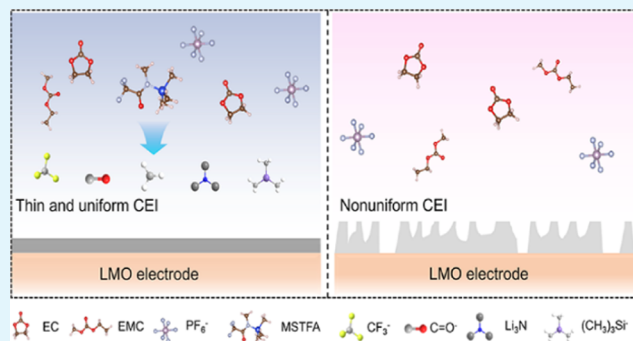
1. INTRODUCTION

Nowadays, lithium-ion batteries (LIBs) are being widely employed as energy storage systems for electric vehicles, portable electronic devices, etc.[1−3] Nevertheless, the energy density and life span performance of electrochemical energy storage equipment cannot satisfy both the economic and environmental requirements.[4−6] Specifically, the cathode material is currently one of the main limiting factors for LIBs. Among those candidate materials,[3,7] the lithium-rich manganese oxide cathode shows an ultrahigh specific capacity of 250 mAh g^{-1} and an average discharge voltage of above 3.5 V. Notably, the lithium-rich manganese oxide (LMO) cathode alleviates the reliance on the costly cobalt, offering also more advantages such as environmental friendliness and excellent thermal stability.[8] However, such high capacity of LMO is accompanied by structural instability.[9−11] In general, LMO can be represented as x Li$_2$MnO$_3$·$(1 − x)$ LiMO$_2$ (M denotes Mn, Co, and Ni),[12] wherein Li$_2$MnO$_3$ provides an extra capacity via redox of the lattice oxygen at high voltage (>4.5 V).[13] Unfortunately, such oxygen redox reactions tend to release highly active compounds that lead to severe side reactions on the LMO surface.[14−16] In detail, the oxygen extracted from the lattice reacted easily with the ring-structure solvents (such as EC or other carbonate solvents). Then, the byproducts like CO$_2$ and H$_2$O are formed.[17] What's worse, these byproducts accelerate the hydrolysis of LiPF$_6$, resulting in the production

of HF acid, which in turn severely corrodes LMO and promotes the dissolution of transition metals.[18,19] Many strategies have been employed to alleviate this challenge. Besides modifying LMO itself, surface modification has been employed to minimize the undesired reactions.[20,21] A stable cathode-electrolyte interphase constructed during material synthesis can effectively suppress irreversible structural transformations and interface side reactions.[22,23] The formation of the cathode-electrolyte interphase (CEI) has received extensive attention, but there are no reports concerning the precise formation mechanism. For the LMO cathode, nucleophilic reaction is probably the key mechanism to induce the CEI film.[24−26] Nevertheless, regulating CEI by introducing electrolyte additives has been regarded as a convenient and efficient strategy to harvest a long-life LMO cathode.[27,28] The components and structure of additives were found to affect the formation of CEI. For example, amide compounds have been utilized because of their superior stability compared to organic carbonates and a range of linear and cyclic ethers.[29]
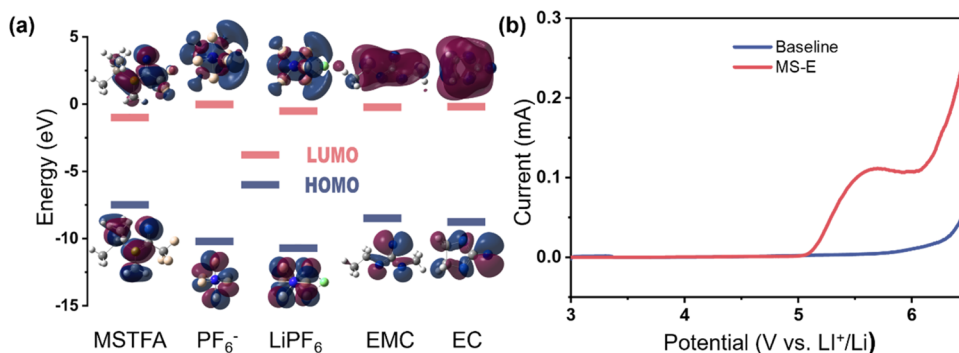
Figure 1. (a) LUMO−HOMO level of various molecules in MS-E. (b) Oxidation potential of Baseline and MS-E characterized by LSV at a scan rate of 0.1 mV s^{-1} from 3 to 6.5 V.

Subsequent studies have further elucidated that amide compounds can facilitate constructing a highly conductive and stable solid electrolyte interface (SEI) in lithium-ion battery systems.[30] Fluorine-containing compounds can enhance the electrolyte's cathodic compatibility at high voltage, as well as improve CEI ionic conductivity and stability.[31] Additionally, silicon-based additives can enhance the interface conductance and stability via building an Si−O−R interphase cathode.[32] In general, additives in electrolyte systems have attracted wide attention. However, as the operating voltage expands, the related working condition becomes more complex and challenging to control.[33,34] Therefore, multifunctional additives are needed to adapt to the high-voltage condition. For example, combining the unsaturated bonds and Si-based functional groups can enhance the electrochemical reaction activity and facilitate building interface surface passivation layers.[35] N,O-bis(trimethylsilyl) trifluoroacetamide as an electrolyte additive shows gratified performance on sodium metal batteries (SMBs) by stabilizing the electrolyte and fabricating a highly conductive interface in SMBs.[36,37] N-tert-butyl-2-thiophenesulfonamide helps to realize a wide-temperature LIBs via building a stable CEI.[38]

In this work, a multifunctional organic molecule (MSTFA) is introduced as an additive in a common carbonate electrolyte (1 M LiPF$_6$ in ethylene carbonate (EC)/ethyl methyl carbonate (EMC) 3:7 vol %, named Baseline, and the electrolyte with MSTFA, named MS-E) for LIBs. The transmission electron microscopy (TEM) and X-ray photoelectron spectroscopy (XPS) results demonstrate that the addition of MSTFA is conducive to build a silicon-base, NO$_x$-contained, thinner, and stable CEI. Benefiting from the modified CEI, the capacity retention of the LMO cathode increases from 81.2 to 92.0% at 250 mA g^{-1} after 100 cycles and improves from 62.4 to 93.1% after 200 cycles at 100 mA g.$^{-1}$ In short, by introducing the additive to construct a stable CEI at high voltage, we architected a stabilized lithium-rich manganese-based oxide cathode for LIBs.

2. EXPERIMENTAL PART

2.1. Preparation of the Electrolyte and Electrode.
LMO material was purchased from the Youyan platform; MSTFA was supplied by Sigma-Aldrich, and the basic solvent was purchased online from Duoduo Reagent. The binder poly(vinylidene fluoride) (PVDF900) was produced by ARKEMA. Conductive carbon black (Super P), metal Li-negative electrodes, and diaphragm were purchased from Canrd Mall.

The LMO cathode was prepared with the active LMO:conductive agent (Super P):binder (PVDF) amount ratio of 8:1:1. Initially, the

active material binder and conductive agent were placed in a 60° oven to dry for 48 h. After completely drying, uniformly ground LMO and Super P were placed in the mortar according to the proportion, and then the appropriate amount of N-methylpyrrolidone (NMP) was added. The mixtures were transferred to an automatic homogenizer for stirring in 20 min at a speed of 2000 r min^{-1}. Then, the uniform conductive paste was coated at a thickness of 100 μm on an Al foil. The LMO cathode was obtained after drying overnight. The baseline was 1 M LiPF$_6$ in EC and EMC (3:7 in vol). MS-E was separated by adding different amounts of MSTFA (1, 2, and 4 wt %) into the baseline. The button battery was assembled according to the order positive shell, positive electrode, electrolyte, diaphragm, electrolyte, gasket, shrapnel, and negative shell. The electrolyte deployment and battery packaging process were both carried out in a glovebox with water and oxygen contents of <0.01 ppm.

2.2. Electrochemical Measurement.
All electrochemical performances without separate mention were tested in Li‖LMO cells with a working window of 2−4.8 V. Cycling performances were analyzed at a current density of 100 and 250 mA g^{-1}. Rate performance was measured at 0.1, 0.5, 1, and 1.5 C (1 C = 200 mAh g^{-1}). The galvanostatic charge/discharge (GCD) tests and galvanostatic intermittent titration technique (GITT) tests were carried out using the Neware Battery test system (CT-4008T) at 25 °C. Cyclic voltammetry (CV) curves were recorded with scan rates of 0.1, 0.3, 0.5, 0.7, and 1 mV s^{-1} on an electrochemical workstation (ivium-vertex. ONE). Electrochemical impedance spectroscopy (EIS) measurements were carried out from 100,000 to 0.01 Hz with an alternate current amplitude of 10 mV using the Admiral electrochemical workstation (Squidstat Plus). Linear sweep voltammetry was performed in a three-electrode system with an electric potential range of 3−6.5 V (Pt foil used as the working electrode and lithium−metal electrode used as the reference electrode and counter electrode) on a CHI660E electrochemical workstation in a glovebox filled with Ar gas at room temperature.

2.3. Material Characterization.
Field emission scanning electron microscopy (SEM) (SU-8010) and HRTEM (JEM-2100F) were used to observe the material morphology, sample size, and lattice fringe. The element composition of the sample was observed by energy dispersive X-ray spectroscopy equipped with FESEM and HRTEM. A Bruker D8X was used to conduct X-ray diffraction (XRD) analysis of the powder samples and electrodes. Cu Kα with a wavelength of 0.15 nm was used as the ray source, and the powder samples and electrodes were tested at the rate of 4° min^{-1} in the range of 10−80°. The XPS instrument used was ESCALAB250 of Thermo Fisher Scientific Company: Al Kα X-ray was used as the ray source; the vacuum was <10^{-8} Pa; the working voltage was 12 kV; the working current was 20 mA; and the energy of the detector was 0.1 eV. Finally, the corresponding software was used to fit the results. The time-of-flight secondary ion mass spectrometry (TOF-SIMS) was done using TESCAN S9000G equipped with a TESCAN C-TOF. An atomic force microscope (AFM, Bruker-Dimension Fast Scan) was used to characterize the surface morphology of the electrode.
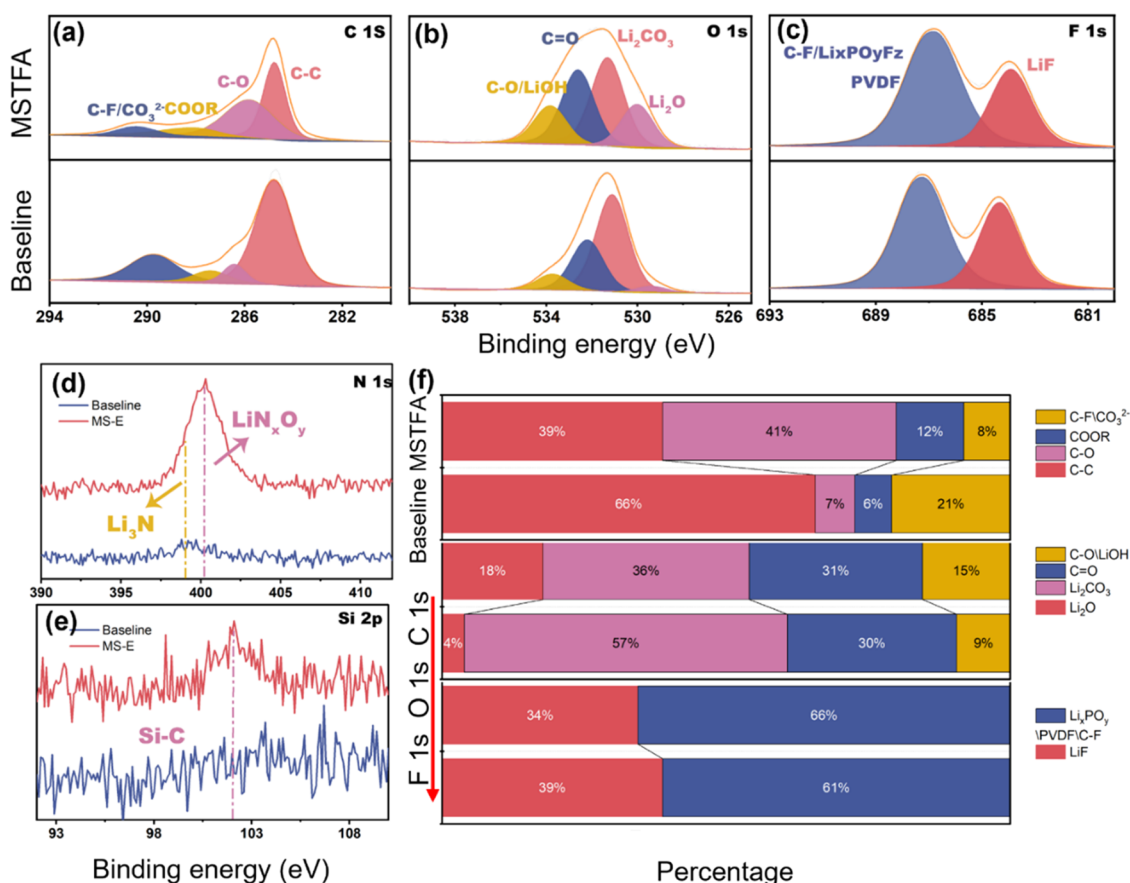
Figure 2. XPS characterization of the cycled LMO cathode in MSTFA and Baseline; XPS fitting peak of C 1s (a), O 1s (b), and F 1s (c); XPS peak of N 1s (d) and Si 2p (e). Quantitative results of C 1s, O 1s, and F 1s (f).

2.4. Computational Details. The geometry of an isolated molecule and complexes was optimized at the B3LYP-D3(BJ)/6-311++G (d, p) level[39,40] using the Gaussian 09 software package. To simulate the solvent environment, the polarizable continuum model (PCM) was employed in all calculations with a dielectric constant of 46, representing the mixed solvent of EC and EMC (1:1, v/v).

3. RESULTS AND DISCUSSION

The frontier molecular orbital energy levels can be used to assess the redox stability of materials. Therefore, the highest occupied molecular orbital (HOMO) and the lowest unoccupied molecular orbital (LUMO) of all electrolyte compounds were calculated using density functional theory (DFT). As shown in Figure 1a, MSTFA has the highest HOMO energy level at −7.45 eV, indicating the tendency of preferential oxidation decomposition. The linear sweep voltammetry (LSV) measurement was employed to further evaluate the redox stability of Baseline and MS-E using a three-electrode system (Li as the counter and reference electrode, Pt as the working electrode). Figure 1b shows a lower oxidation potential (4.974 V) in MS-E, demonstrating that prior oxidative decomposition actually occurs. Meanwhile, LSV toward the negative side is shown in Figure S1; the electrolyte with MSTFA added has an obvious reduction peak at 1.039 V, while the reduction peak of baseline above 0.5 V is unobvious. The results of LSV tie well with the calculations described above. The initial CV is shown in Figure S2, and a strong oxidation peak above 4.5 V can be seen in both MS-E and Baseline. The current intensity caused by the oxygen oxidation reaction of Li_2MnO_3 in MS-E is smaller. This means the

introduction of MSTFA may have an effect on the reactive oxygen species on the LMO surface. Consequently, MSTFA is preferentially oxidized to participate in the formation of CEI.

To further exploit the effect of MSTFA, a gradient electrolyte was generated by introducing 1, 2, and 4 wt % MSTFA into Baseline. The initial impedance demonstrates a decrease with an increasing additive concentration. With 2 and 4 wt % MSTFA addition, the R_{ct} of LMO decreases to 42.7% and 73.0%, respectively (Figure S3). The sample in the 2 wt % MSTFA electrolyte exhibits the best cycling performance (Figure S4), which was selected for further verification.

Cycled LMO cathodes were disassembled to further investigate the cyclic failure caused by structural evolution. X-ray diffraction (XRD) tests were performed to analyze the structure of the cathode first. Generally, LMO is expressed as x $Li_2MnO_3 \cdot (1 − x)$ $LiMO_2$. Due to the similar structure of two constituting phases, the patterns of LMO can be indexed to α-$NaFeO_2$ hexagonal structure ($R\bar{3}m$) except for the weak reflections at 20−25°, ascribed to Li_2MnO_3 ($C2/m$).[36] Figure S5 shows the standard XRD pattern of LMO, which could be well fitted by monoclinic ($C2/m$ for Li_2MnO_3, JCPDS No. 24−0734) or trigonal structure ($R\bar{3}m$ for $LiMO_2$, JCPDS No. 09−0063).[12,41] The close-packed layers in each of these compounds ((001) monoclinic and (003) trigonal) have an interlayer with the spacing close to 4.7 Å (corresponding to 18.7°). After 200 cycles, the main peaks of LMO remain in terms of both MS-E and Baseline; that is, no obvious phase transition reaction has occurred during cycling (Figure S6). Subsequently, scanning electron microscopy (SEM) was
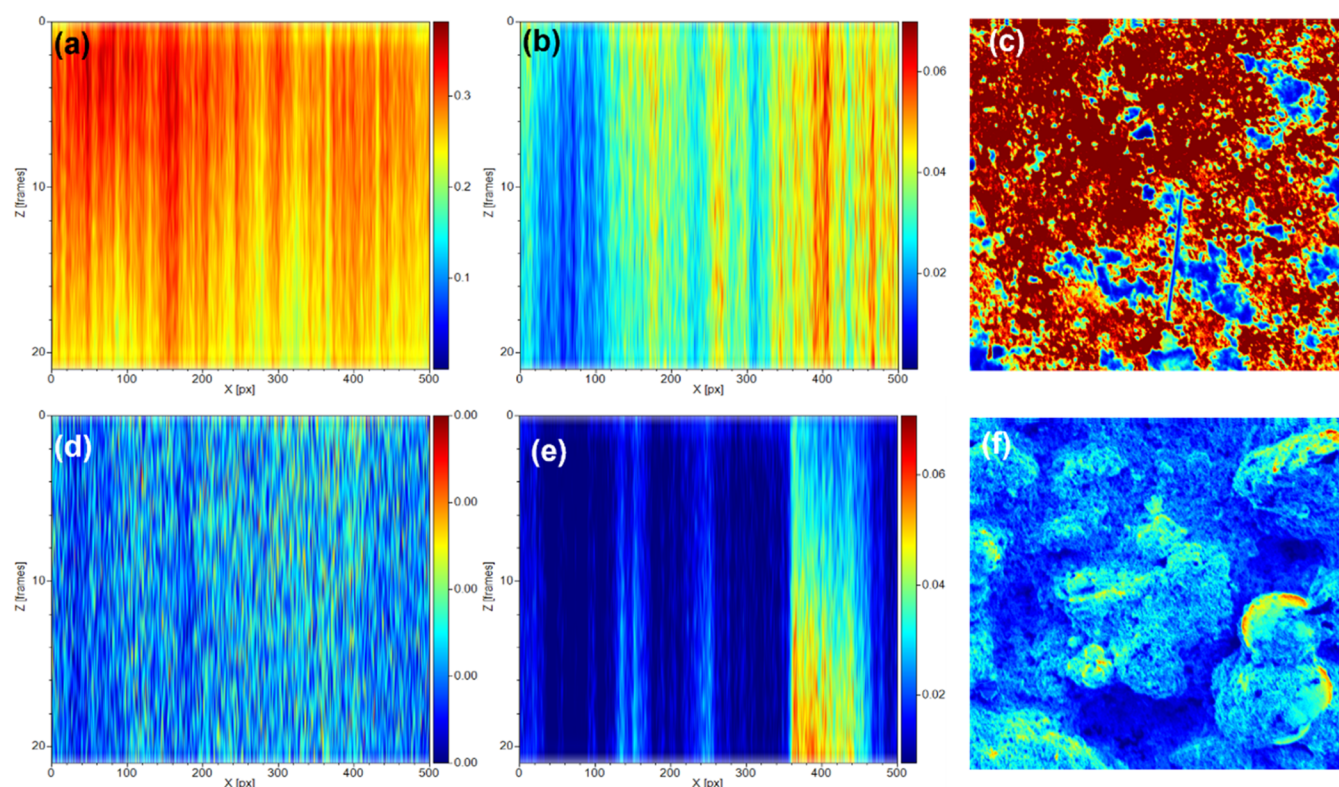
Figure 3. TOF-SIMS profiling of several ions on the LMO surface in MS-E and Baseline, respectively. TOF-SIMS results of (a, d) F ion and (b, e) O ion in the depth direction. (c, f) Focused Ion Beam (FIB)-SEM image with a range of 40 μm × 40 μm.

employed to observe the surface morphology of the cycled LMO cathode in different electrolytes. The detailed results reveal that the MSTFA additive maintained the spherical morphology of LMO, in contrast to the fractured and pulverized surface in Baseline that appeared (Figure S7). This is also consistent with the results of the AFM data (Figure S8). Meanwhile, the energy dispersive spectroscopy (EDS) elemental maps (Figure S9) indicate that the surface composition of LMO has changed due to the addition of MSTFA.

The surface chemical composition and proportions of the LMO cathode in different electrolytes were probed by X-ray photoelectron spectroscopy (XPS). Figure 2a−c shows the XPS fitting peaks of C 1s, O 1s, and F 1s, respectively. There are four peaks in the C 1s spectrum, as the C−C bond at 284.8, C−O at 285.9, COOR at 288.2, and C−F/CO$_3^{2-}$ bond at 290.4 eV.[42−44] O 1s spectra can be found to hold four main peaks in Figure 2b, with the one at 530 eV attributed to Li$_2$O bonding from the oxygenated surface species; at 532.6 eV C═O, and at 531.3 eV Li$_2$CO$_3$ and C−O bonding are found.[41] As a matter of fact, the unstable interphase of Li$_2$CO$_3$ in the LMO cathode is less in MS-E, while Li$_2$CO$_3$ is regarded as an unstable component in cycling. The quantitative results of O 1s peak show that the content of Li$_2$CO$_3$ in MS-E was 36%, lower than that in Baseline (57%), which is also demonstrated by the quantitative results of the C 1s peak (Figure 2f). The mass ratio of carbon to oxygen also decreased with the MSTFA addition, which indicates that the decomposition components of the electrolyte solvent are reduced for participating in the CEI architecture.[13] The LiF peak at 684.7 eV is contributed by the broken scenarios of C−F in MS-E and anion decomposition. The higher binding energy of 687.8 eV comes from P−F in Li$_x$PO$_y$ and PVDF. The quantitative results of F 1s and

the mass ratio of F content (28% in MS-E and 16% in Baseline, respectively, Figure S10) indicate that the LMO in MS-E contains almost double the LiF content on the surface. Commonly, LiF is considered a beneficial inorganic component in the CEI, which can promote the Li-ion interfacial transportation.[37] On the other hand, Figures 2d and S11 show that LMO has an additional 2p peak of Si in MS-E, indicating that the silicon-base component from the decomposition of MSTFA participated in the construction of CEI. Silicon-based components are regarded as a booster to enhance the interface conductance and stability via building the Si−O−R bond. In addition, the N 1s signal in MS-E demonstrates that the CEI contains Li$_3$N (398.9 eV) and LiN$_x$O$_y$ (400.3 eV) in MS-E. Li$_3$N appearing in Baseline is considered as the product formed by the Li ion in the cathode reacting with the N$_2$ in air during testing.[44] The mass quantitative ratio of elements also shows that the sample in MS-E has a higher N content (3%, corresponding to 1% in Baseline). LiN$_x$O$_y$ and silicon-based components are confirmed to have lower Li$^+$ diffusion energy barriers. Additionally, the results of rich F and N in CEI for MS-E are consistent with the energy dispersive spectroscopy (EDS) results (Figure S12). Generally, the CEI formed in MS-E has the characteristics of being LiF-rich and containing Si/N functional groups, which is beneficial to cathode stability.

TOF-SIMS was performed to evaluate the compositional distribution in the CEI on the cycled LMO. The LMO in MS-E has a fluorine-rich surface (Figure 3a,d). In line with the XPS results mentioned above, an LiF-rich CEI was formed on the LMO in MS-E.

For further investigation of the characteristics of the cycled LMO electrodes, transmission electron microscopy was employed. As depicted in Figure 4a, the LMO cathode in
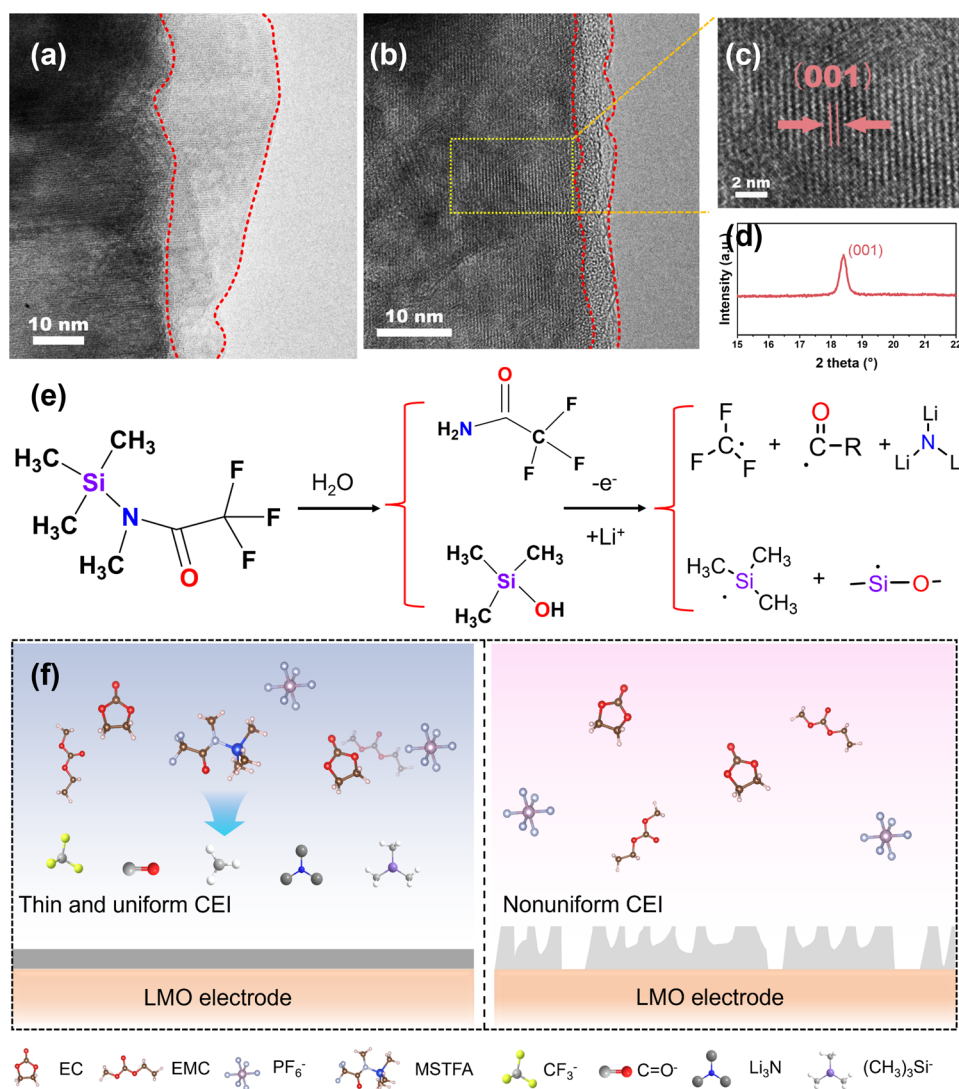
Figure 4. HRTEM images of LMO particles in the baseline (a) and MS-E (b) electrolytes after 200 cycles. (c) Enlarged image from (b). (d) XRD patterns of LMO after cycles. (e) Illustrating decomposition path of MSTFA. (f) Working mechanism of the MSTFA additive.

Baseline shows a thick and uneven CEI with thickness from 8.8 to 24.4 nm. Conversely, the introduction of additives yields a uniform and dense CEI of ∼4.3 nm (Figure 4b). What's more, Figure 4c shows (001) planes of Li_2MnO_3, which is well in correspondence with the above XRD data. Combined with the analysis of XPS and the decomposition pathway, a possible decomposition path of MSTFA is proposed (Figure 4e). The calculation results indicate that MSTFA will undergo a series of chemical bond breaks around the N atom.[43] MSTFA may react with water to form trimethylsilanol and acetamide.

Then, trimethylsilanol and acetamide will further break down into small molecules containing F, N, and Si. As shown in Figure 4f, a dense and uniform CEI will be formed via the participation of the small molecules. On the contrary, the common electrolyte forms a nonuniform and unstable CEI because of the side reaction between the electrolyte solvent and the electrode.

Comprehensive electrochemical characterizations were performed to evaluate the kinetics of Li ions migrating beneath the CEI. Electrochemical impedance spectroscopy (EIS) can achieve the in situ detection of the complex reaction process inside a battery.[45] The EIS of the cycled LMO cathode

was tested first to evaluate the ability of charge transfer. As a consequence, the impedance of the LMO cathode in MS-E (R_{ct} = 51.2 Ω) electrolyte is much lower than that in Baseline (136 Ω) (Figure 5a). According to the Arrhenius formula, the activation energy of the electrode can be obtained by measuring the impedance at different temperatures. In this work, EIS curves mainly contain two depressed semicircles at high and medium frequencies and a diagonal line at low frequency. It has been well accepted that the depressed semicircle reveals the reaction resistance of the surface film (R_{CEI}) and charge transfer (R_{ct}).[46] Therefore, the activation energy for Li-ion diffusion through the CEI was further investigated by temperature-dependent EIS in the range of 300−330 K (Figures 5b and S13). As a result, the activation energy in MS-E is 14.68 kJ mol^{-1}, less than that in Baseline (16.91 kJ mol^{-1}). The fast kinetics of Li-ion diffusion in the CEI constructed in MS-E is due to the Si and N molecules from the MSTFA decomposition. What's more, the activation energy for Li-ion diffusion through the whole cathode was further investigated. The activation energy in MS-E is 19.29 kJ mol^{-1}, less than that in Baseline (24.61 kJ mol^{-1}, Figure S14). Consequently, the faster kinetics of diffusion contributed to the
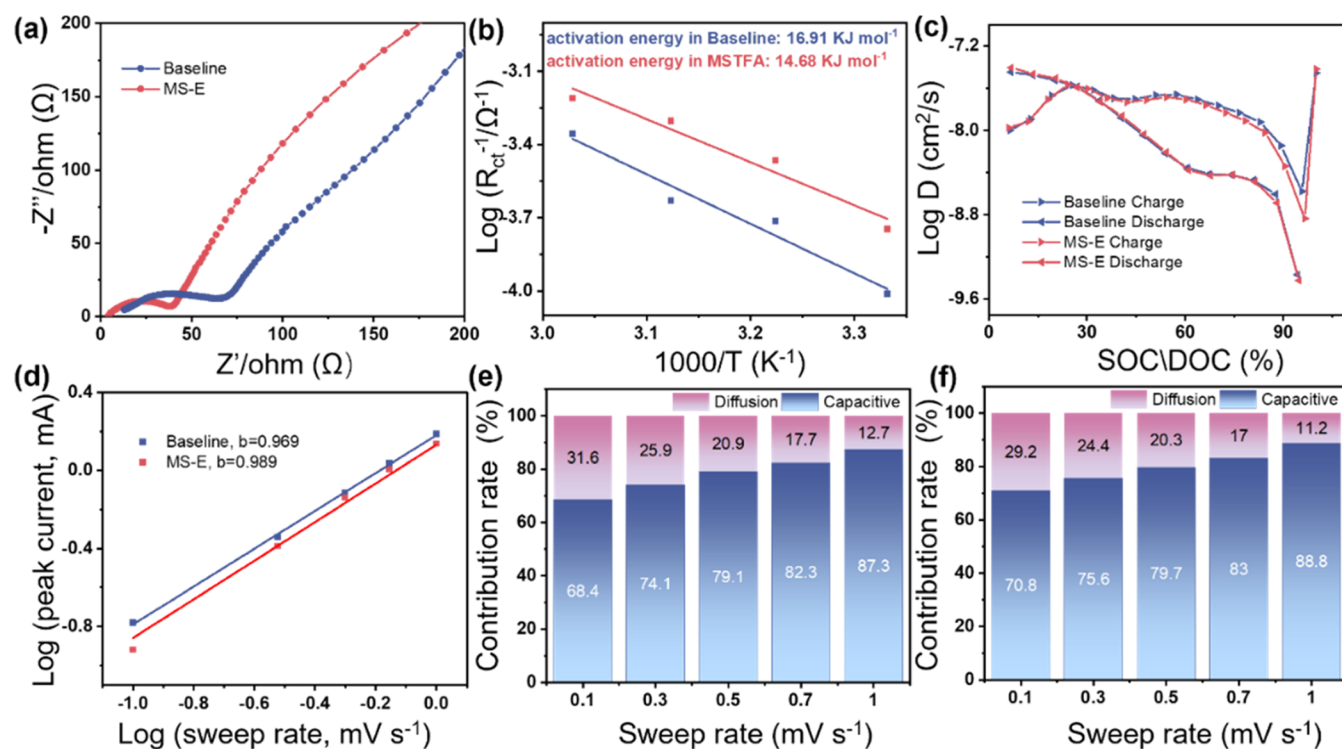
Figure 5. Electrochemical kinetics of the LMO cathode in MS-E and Baseline. (a) EIS curves after 200 cycles. (b) CEI activation energy in different electrolytes. (c) GITT analysis of the LMO cathode. (d) $\log i$ vs $\log v$ plots and fitting lines at the current peak based on CV curves. The contribution ratio bar chart of capacitive and diffusion-controlled capacities at different scan rates of LMO in Baseline (e) and MS-E (f).
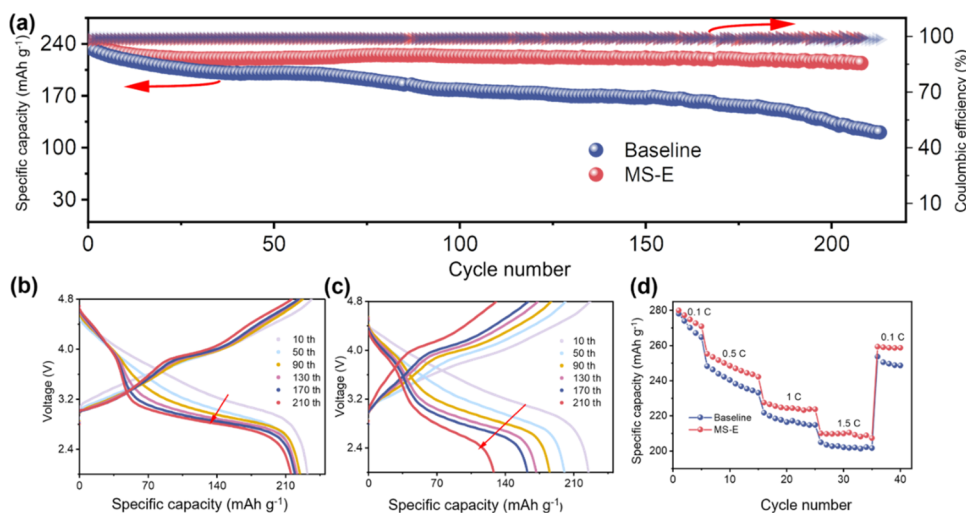
Figure 6. Electrochemical performance of the Li‖LMO cells at 25 °C. (a) Cycling performance at 0.5 C. Charge−discharge profiles of different cycles using MS-E (b) and the baseline (c). (d) Rate performance for different electrolytes.

higher Li-ion concentration beneath LMO under the same reaction rate, thus improving the reversibility of the cathodic redox reaction. The lithium chemical diffusion coefficient was further calculated by the galvanostatic intermittent titration technique (GITT).[47] GITT is easy to implement and universally accepted as the standard for solid-phase diffusivity measurement. The GITT diffusivity formula is given by

$$D_s = \frac{4}{\pi\tau}\left(\frac{n_M V_M}{S}\right)^2\left(\frac{\Delta V_s}{\Delta V_t}\right)^2$$

where n_M and V_M are the molar mass and molar volume of the active material, respectively, S is the cell interfacial area, and τ is the time duration of the pulse.

As shown in Figures 5c and S15, D_{Li} calculated based on GITT data has little difference between MS-E and Baseline. It means Li-ion diffusion in the inner phase of the LMO cathode is not seriously modified, and the MSTFA mainly affects LMO's surface.[48] Furthermore, a series of CV measurements for the LMO cathode were collected at various scan rates ranging from 0.1 to 1 mV s^{-1}. The relevant kinetic information was obtained from CV measurements (Figure S16). For a redox reaction limited by semi-infinite diffusion, the peak

current i varies as $v^{1/2}$ (v is the scan rate); for a capacitive process,[49] it varies as v. This relation is expressed as $i = av^b$. As a result, both of the calculated b values in MS-E were near 1, but the LMO in MS-E (0.989) is higher than in Baseline (0.969). The higher b value indicates that the LMO in MS-E exhibits more capacitor behavior. For a deeper investigation, the current response (i) at a fixed potential (V) can be described as the combination of two separate mechanisms,[50] namely capacitive effects (k_1v) and diffusion-controlled insertion ($k_2v^{1/2}$), according to $i(V) = k_1v + k_2v^{1/2}$ (Figure 5d). As shown in Figure 5e,f, this method is used to distinguish the fraction of the current arising from Li$^+$ insertion from the capacitive processes at specific potentials. As a result, the LMO cathode in MS-E has a higher capacitive contribution, and at the sweep rate of 0.1 mV s^{-1}, a maximum capacitive-controlled ratio of 70.8% is achieved in MS-E, higher than that in Baseline (68.4%). It reveals a faster ionic diffusion kinetics in the MS-E, indicating that the LMO cathode has optimal dynamic behavior in the MS-E.[51] In short, our results demonstrated that a CEI modified by MS-E has faster kinetics of diffusion.

To further validate the functionality of the MS-E, electrochemical performance testing was performed in MS-E and Baseline. The introduction of MSTFA increases the capacity retention of LMO from 62.4 to 93.1% after 200 cycles at a density of 100 mA g^{-1} (Figure 6a). The Coulomb efficiency (C.E.) of MS-E can reach 99.2%, surpassing the baseline (98.18%). Differential-capacity profiles (dQ/dV) of selected cycles also show that MSTFA improves the redox reversibility of LMO (Figure S17).

In addition, Figure S18 shows that the reversibility of LMO is also improved at 250 mA g^{-1} (with 2% MSTFA addition, the capacity retention of the LMO cathode increases from 81.2 to 92.0% after 100 cycles), indicating that the designed CEI can protect the surface of LMO at a larger current density. This is consistent with the aforementioned characterization that LMO in MS-E has faster kinetics of diffusion. Meanwhile, a performance comparison and parallel test data are given in Figures S19−S21. In short, MSTFA can boost the stability of the LMO cathode at a wide-range working window and a high cutoff potential (4.8 V). What's more, as shown in Figure 6d, the rate performance is also excellent using MS-E; LMO displays the capacities of 270.9, 248.5, 224.4, and 209.9 mAh g^{-1} at 0.1, 0.5, 1, and 1.5 C, respectively (1 C = 200 mAh g^{-1}), higher than that in Baseline (264.77, 240.39, 216.51, and 202.19 mAh g^{-1}, correspondingly). This corroborates the kinetics enhancement mentioned above that CEI regulated by MSTFA is more conducive to the transport of Li ions. Generally, as MSTFA can induce a thin and homogeneous CEI, LMO can provide stable and high electrochemical performance.

4. CONCLUSIONS

In conclusion, by inducing MSTFA into the electrolyte, electrolyte oxidative decomposition at high voltage is effectively mitigated, resulting in the preferential formation of a thin and stable CEI film on the LMO cathode. First, we proved the feasibility of MSTFA as a film-forming additive by combining theoretical calculations with electrochemical experiments. Then, a series of performance and characterization tests were performed. The results of XPS and TOF-SIMS show that there are LiF-rich, silicon, and nitrogen functional groups on the LMO surface. Meanwhile, TEM shows that a thin and

uniform CEI is constructed on the LMO cathode in MS-E. In addition, the dynamics tests show that the LMO cathode with the designed CEI has an optimal kinetics, which is in line with the results of rate performance. Moreover, at the current density of 250 mA g^{-1}, the capacity retention of LMO cathode increased from 81.2 to 92.0% after 100 cycles, and improved from 62.4 to 93.1% after 200 cycles at 100 mA g^{-1}. Our study highlights the potential for regulating CEI through the addition of an additive in high-voltage systems.

■ ASSOCIATED CONTENT

Ⓢ Supporting Information

The Supporting Information is available free of charge at https://pubs.acs.org/doi/10.1021/acsaem.3c03224.

Reduction potential of various electrolytes characterized by LSV at a scan rate of −0.1 mV s^{-1} from 3 to 0.01 V; first two cycle CV curves of LMO cathode in MS-E and in Baseline; initial impedance of LMO cathode with gradient electrolyte; cycling performance of LMO cathode with gradient electrolyte at 250 mA g^{-1}; XRD pattern of LMO and corresponding structure fitting by standard PDF card; XRD patterns of cycled LMO cathode in MS-E and Baseline; SEM images of cycled LMO cathode in MS-E and Baseline; AFM images of cycled LMO cathode in MS-E and Baseline; EDS elemental maps associated with SEM observation; elemental quantification (mass ratio) results of cycled LMO cathode in Baseline and MS-E according to XPS peak; full XPS profiles of cycled LMO cathode in Baseline and MS-E; EDS elemental maps for cycled LMO cathode associated with TEM observation; EIS curve of LMO cathode at different temperatures; the activation energy of the whole cathode according to EIS curves at different temperatures; GITT curve and corresponding calculated lg D of LMO cathode; CV curves of LMO cathode; differential-capacity profiles (dQ/dV) of LMO cathode in Baseline and MS-E; cycling performance of LMO in Baseline and MS-E at 250 mA g^{-1}; cycling performance comparison with others work; parallel test of cycling performance; predicted capacity of 500th cycled via capacity decay rate (PDF)

■ AUTHOR INFORMATION

Corresponding Authors

Dong Wang − *Key Laboratory of Automobile Materials of MOE, and School of Materials Science and Engineering, and Electron Microscopy Center, and International Center of Future Science, and Jilin Provincial International Cooperation Key Laboratory of High-Efficiency Clean Energy Materials, Jilin University, Changchun 130012, P. R. China;* ⓞ orcid.org/0000-0003-2456-6175; Email: wangdong2023@jlu.edu.cn

Wei Zhang − *Key Laboratory of Automobile Materials of MOE, and School of Materials Science and Engineering, and Electron Microscopy Center, and International Center of Future Science, and Jilin Provincial International Cooperation Key Laboratory of High-Efficiency Clean Energy Materials, Jilin University, Changchun 130012, P. R. China;* ⓞ orcid.org/0000-0002-6414-7015; Email: weizhang@jlu.edu.cn

Authors

Zhuoran Feng − *Key Laboratory of Automobile Materials of MOE, and School of Materials Science and Engineering, and Electron Microscopy Center, and International Center of Future Science, and Jilin Provincial International Cooperation Key Laboratory of High-Efficiency Clean Energy Materials, Jilin University, Changchun 130012, P. R. China*

Leyi Guo − *Key Laboratory of Automobile Materials of MOE, and School of Materials Science and Engineering, and Electron Microscopy Center, and International Center of Future Science, and Jilin Provincial International Cooperation Key Laboratory of High-Efficiency Clean Energy Materials, Jilin University, Changchun 130012, P. R. China*

Xiaofei Liu − *Key Laboratory of Automobile Materials of MOE, and School of Materials Science and Engineering, and Electron Microscopy Center, and International Center of Future Science, and Jilin Provincial International Cooperation Key Laboratory of High-Efficiency Clean Energy Materials, Jilin University, Changchun 130012, P. R. China*

Wenwen Li − *Key Laboratory of Automobile Materials of MOE, and School of Materials Science and Engineering, and Electron Microscopy Center, and International Center of Future Science, and Jilin Provincial International Cooperation Key Laboratory of High-Efficiency Clean Energy Materials, Jilin University, Changchun 130012, P. R. China*

Ruipeng Zhang − *Key Laboratory of Automobile Materials of MOE, and School of Materials Science and Engineering, and Electron Microscopy Center, and International Center of Future Science, and Jilin Provincial International Cooperation Key Laboratory of High-Efficiency Clean Energy Materials, Jilin University, Changchun 130012, P. R. China*

Weitao Zheng − *Key Laboratory of Automobile Materials of MOE, and School of Materials Science and Engineering, and Electron Microscopy Center, and International Center of Future Science, and Jilin Provincial International Cooperation Key Laboratory of High-Efficiency Clean Energy Materials, Jilin University, Changchun 130012, P. R. China*

Complete contact information is available at:
https://pubs.acs.org/10.1021/acsaem.3c03224

Notes

The authors declare no competing financial interest.

■ REFERENCES

(1) Xie, J.; Lu, Y.-C. A retrospective on lithium-ion batteries. *Nat. Commun.* **2020**, *11* (1), No. 2499.

(2) Goodenough, J. B.; Park, K.-S. The Li-Ion Rechargeable Battery: A Perspective. *J. Am. Chem. Soc.* **2013**, *135* (4), 1167−1176.

(3) Dogan, F.; Long, B. R.; Croy, J. R.; Gallagher, K. G.; Iddir, H.; Russell, J. T.; Balasubramanian, M.; Key, B. Re-entrant Lithium Local Environments and Defect Driven Electrochemistry of Li- and Mn-Rich Li-Ion Battery Cathodes. *J. Am. Chem. Soc.* **2015**, *137* (6), 2328−2335.

(4) Manzetti, S.; Mariasiu, F. Electric vehicle battery technologies: From present state to future systems. *Renewable Sustainable Energy Rev.* **2015**, *51*, 1004−1012.

(5) Li, M.; Lu, J.; Chen, Z.; Amine, K. 30 Years of Lithium-Ion Batteries. *Adv. Mater.* **2018**, *30* (33), No. 1800561.

(6) Zhang, W.; Wang, D.; Zheng, W. A semiconductor-electrochemistry model for design of high-rate Li ion battery. *J. Energy Chem.* **2020**, *41*, 100−106.

(7) Manthiram, A.; Knight, J. C.; Myung, S.-T.; Oh, S.-M.; Sun, Y.-K. Nickel-Rich and Lithium-Rich Layered Oxide Cathodes: Progress and Perspectives. *Adv. Energy Mater.* **2016**, *6* (1), No. 1501010.

(8) Wang, J.; He, X.; Paillard, E.; Laszczynski, N.; Li, J.; Passerini, S. Lithium- and Manganese-Rich Oxide Cathode Materials for High-Energy Lithium Ion Batteries. *Adv. Energy Mater.* **2016**, *6* (21), No. 1600906.

(9) Wu, Y.; Manthiram, A. Effect of surface modifications on the layered solid solution cathodes $(1-z)$ $Li[Li_{1/3}Mn_{2/3}]O_2-(z)$ $Li[Mn_{0.5-y}Ni_{0.5-y}Co_{2y}]O_2$. *Solid State Ionics* **2009**, *180* (1), 50−56.

(10) Qian, D.; Xu, B.; Chi, M.; Meng, Y. S. Uncovering the roles of oxygen vacancies in cation migration in lithium excess layered oxides. *Phys. Chem. Chem. Phys.* **2014**, *16* (28), 14665−14668.

(11) Yabuuchi, N.; Yoshii, K.; Myung, S.-T.; Nakai, I.; Komaba, S. Detailed Studies of a High-Capacity Electrode Material for Rechargeable Batteries, $Li_2MnO_3-LiCo_{1/3}Ni_{1/3}Mn_{1/3}O_2$. *J. Am. Chem. Soc.* **2011**, *133* (12), 4404−4419.

(12) Thackeray, M. M.; Kang, S.-H.; Johnson, C. S.; Vaughey, J. T.; Benedek, R.; Hackney, S. A. Li_2MnO_3-stabilized $LiMO_2$ (M = Mn, Ni, Co) electrodes for lithium-ion batteries. *J. Mater. Chem.* **2007**, *17* (30), 3112−3125.

(13) Gao, X.; Zhang, H.; Li, S.; Zhang, S.; Guan, C.; Hu, X.; Guo, J.; Lai, Y.; Zhang, Z. Local Electronic Structure Modulation Enables Fast-Charging Capability for Li-Rich Mn-Based Oxides Cathodes With Reversible Anionic Redox Activity. *Adv. Funct. Mater.* **2023**, *33* (43), No. 2304065.

(14) Lu, Z.; MacNeil, D. D.; Dahn, J. R. Layered Cathode Materials $Li[Ni_x Li_{(1/3-2x/3)}Mn_{(2/3-x/3)}]O_2$ for Lithium-Ion Batteries. *Electrochem. Solid-State Lett.* **2001**, *4* (11), No. A191, DOI: 10.1149/1.1407994.

(15) Amalraj, S. F.; Markovsky, B.; Sharon, D.; Talianker, M.; Zinigrad, E.; Persky, R.; Haik, O.; Grinblat, J.; Lampert, J.; Schulz-Dobrick, M.; Garsuch, A.; Burlaka, L.; Aurbach, D. Study of the electrochemical behavior of the "inactive" Li_2MnO_3. *Electrochim. Acta* **2012**, *78*, 32−39, DOI: 10.1016/j.electacta.2012.05.144.

(16) Xu, K. Electrolytes and Interphases in Li-Ion Batteries and Beyond. *Chem. Rev.* **2014**, *114* (23), 11503−11618.

(17) Hy, S.; Felix, F.; Rick, J.; Su, W.-N.; Hwang, B. J. Direct In situ Observation of Li_2O Evolution on Li-Rich High-Capacity Cathode Material, $Li[Ni_x Li_{(1-2x)/3}Mn_{(2-x)/3}]O_2$ $(0 \leq x \leq 0.5)$. *J. Am. Chem. Soc.* **2014**, *136* (3), 999−1007.

(18) Fan, Y.; Zhang, W.; Zhao, Y.; Guo, Z.; Cai, Q. Fundamental understanding and practical challenges of lithium-rich oxide cathode materials: Layered and disordered-rocksalt structure. *Energy Storage Mater.* **2021**, *40*, 51−71.

(19) Zhao, J.; Zhang, X.; Liang, Y.; Han, Z.; Liu, S.; Chu, W.; Yu, H. Interphase Engineering by Electrolyte Additives for Lithium-Rich Layered Oxides: Advances and Perspectives. *ACS Energy Lett.* **2021**, *6* (7), 2552−2564.

(20) Wang, Q. Y.; Liu, J.; Murugan, A. V.; Manthiram, A. High capacity double-layer surface modified $Li[Li_{0.2}Mn_{0.54}Ni_{0.13}Co_{0.13}]O_2$ cathode with improved rate capability. *J. Mater. Chem.* **2009**, *19* (28), 4965−4972.

(21) Peng, J.; Li, Y.; Chen, Z.; Liang, G.; Hu, S.; Zhou, T.; Zheng, F.; Pan, Q.; Wang, H.; Li, Q.; Liu, J.; Guo, Z. Phase Compatible $NiFe_2O_4$ Coating Tunes Oxygen Redox in Li-Rich Layered Oxide. *ACS Nano* **2021**, *15* (7), 11607−11618.

(22) Liu, H.; Chen, C.; Du, C.; He, X.; Yin, G.; Song, B.; Zuo, P.; Cheng, X.; Ma, Y.; Gao, Y. Lithium-rich $Li_{1.2}Ni_{0.13}Co_{0.13}Mn_{0.54}O_2$ oxide coated by Li_3PO_4 and carbon nanocomposite layers as high performance cathode materials for lithium ion batteries. *J. Mater. Chem. A* **2015**, *3* (6), 2634−2641.

(23) Dong, T.; Qin, T.; Zhang, W.; Zhang, Y.; Feng, Z.; Gao, Y.; Pan, Z.; Xia, Z.; Wang, Y.; Yang, C.; Wang, P.; Zheng, W. Nature of the electric double layer to modulate the electrochemical behaviors of Fe_2O_3 electrode. *Acta Mater.* **2024**, *263*, No. 119500.

(24) Aurbach, D. Review of selected electrode−solution interactions which determine the performance of Li and Li ion batteries. *J. Power Sources* **2000**, *89* (2), 206−218.

(25) Peled, E. The Electrochemical Behavior of Alkali and Alkaline Earth Metals in Nonaqueous Battery Systems—The Solid Electrolyte Interphase Model. *J. Electrochem. Soc.* **1979**, *126* (12), No. 2047, DOI: 10.1149/1.2128859.

(26) Aurbach, D.; Gamolsky, K.; Markovsky, B.; Salitra, G.; Gofer, Y.; Heider, U.; Oesten, R.; Schmidt, M. The Study of Surface Phenomena Related to Electrochemical Lithium Intercalation into Li_xMO_y Host Materials (M = Ni, Mn). *J. Electrochem. Soc.* **2000**, *147* (4), No. 1322, DOI: 10.1149/1.1393357.

(27) Goodenough, J. B.; Kim, Y. Challenges for Rechargeable Li Batteries. *Chem. Mater.* **2010**, *22* (3), 587−603.

(28) Chen, Y.; He, Q.; Mo, Y.; Zhou, W.; Zhao, Y.; Piao, N.; Liu, C.; Xiao, P.; Liu, H.; Li, B.; Chen, S.; Wang, L.; He, X.; Xing, L.; Liu, J. Engineering an Insoluble Cathode Electrolyte Interphase Enabling High Performance NCM811//Graphite Pouch Cell at 60 °C. *Adv. Energy Mater.* **2022**, *12* (33), No. 2201631.

(29) Chen, Y.; Freunberger, S. A.; Peng, Z.; Bardé, F.; Bruce, P. G. Li−O$_2$ Battery with a Dimethylformamide Electrolyte. *J. Am. Chem. Soc.* **2012**, *134* (18), 7952−7957.

(30) Wang, Q.; Yao, Z.; Zhao, C.; Verhallen, T.; Tabor, D. P.; Liu, M.; Ooms, F.; Kang, F.; Aspuru-Guzik, A.; Hu, Y.-S.; Wagemaker, M.; Li, B. Interface chemistry of an amide electrolyte for highly reversible lithium metal batteries. *Nat. Commun.* **2020**, *11* (1), No. 4188.

(31) Amanchukwu, C. V.; Yu, Z.; Kong, X.; Qin, J.; Cui, Y.; Bao, Z. A New Class of Ionically Conducting Fluorinated Ether Electrolytes with High Electrochemical Stability. *J. Am. Chem. Soc.* **2020**, *142* (16), 7393−7403.

(32) Kim, J.; Adiraju, V. A. K.; Chae, O. B.; Lucht, B. L. Lithium Bis(trimethylsilyl) Phosphate as an Electrolyte Additive to Improve the Low-Temperature Performance for $LiNi_{0.8}Co_{0.1}Mn_{0.1}O_2$/Graphite Cells. *J. Electrochem. Soc.* **2021**, *168* (8), No. 080538, DOI: 10.1149/1945-7111/ac1b00.

(33) Jiang, R.; Hong, L.; Liu, Y.; Wang, Y.; Patel, S.; Feng, X.; Xiang, H. An acetamide additive stabilizing ultra-low concentration electrolyte for long-cycling and high-rate sodium metal battery. *Energy Storage Mater.* **2021**, *42*, 370−379.

(34) Hu, Z.; Wang, K.; Che, Y.; Liu, M.; Zhang, W.; Xing, L.; Wang, H.; Li, S.; Liu, X.; Li, W. A Novel Electrolyte Additive Enables High-Voltage Operation of Nickel-Rich Oxide/Graphite Cells. *J. Phys. Chem. Lett.* **2021**, *12* (18), 4327−4338.

(35) Lan, X.; Yang, S.; Meng, T.; Zhang, C.; Hu, X. A Multifunctional Electrolyte Additive With Solvation Structure Regulation and Electrode/Electrolyte Interface Manipulation Enabling High-Performance Li-Ion Batteries in Wide Temperature Range. *Adv. Energy Mater.* **2023**, *13* (16), No. 2203449.

(36) Wang, C.-C.; Jarvis, K. A.; Ferreira, P. J.; Manthiram, A. Effect of Synthesis Conditions on the First Charge and Reversible Capacities of Lithium-Rich Layered Oxide Cathodes. *Chem. Mater.* **2013**, *25* (15), 3267−3275.

(37) Li, Q.; Wang, Y.; Wang, X.; Sun, X.; Zhang, J.-N.; Yu, X.; Li, H. Investigations on the Fundamental Process of Cathode Electrolyte Interphase Formation and Evolution of High-Voltage Cathodes. *ACS Appl. Mater. Interfaces* **2020**, *12* (2), 2319−2326.

(38) Deng, W.; Dai, W.; Zhou, X.; Han, Q.; Fang, W.; Dong, N.; He, B.; Liu, Z. Competitive Solvation-Induced Concurrent Protection on the Anode and Cathode toward a 400 Wh kg$^{−1}$ Lithium Metal Battery. *ACS Energy Lett.* **2021**, *6* (1), 115−123.

(39) Grimme, S.; Antony, J.; Ehrlich, S.; Krieg, H. A consistent and accurate ab initio parametrization of density functional dispersion correction (DFT-D) for the 94 elements H-Pu. *J. Chem. Phys.* **2010**, *132* (15), No. 154104.

(40) Papajak, E.; Zheng, J.; Xu, X.; Leverentz, H. R.; Truhlar, D. G. Perspectives on Basis Sets Beautiful: Seasonal Plantings of Diffuse Basis Functions. *J. Chem. Theory Comput.* **2011**, *7* (10), 3027−3034.

(41) Lu, Z.; Liu, D.; Dai, K.; Liu, K.; Jing, C.; He, W.; Wang, W.; Zhang, C.; Wei, W. Tailoring solvation chemistry in carbonate electrolytes for all-climate, high-voltage lithium-rich batteries. *Energy Storage Mater.* **2023**, *57*, 316−325.

(42) Ye, C.; Tu, W.; Yin, L.; Zheng, Q.; Wang, C.; Zhong, Y.; Zhang, Y.; Huang, Q.; Xu, K.; Li, W. Converting detrimental HF in electrolytes into a highly fluorinated interphase on cathodes. *J. Mater. Chem. A* **2018**, *6* (36), 17642−17652.

(43) Peng, Q.; Liu, Z.; Chen, S.; Duan, P.; Cheng, S.; Jiang, L.; Sun, J.; Wang, Q. Developing multifunctional amide additive by rational molecular design for high-performance Li metal batteries. *Nano Energy* **2023**, *113* (3), No. 108547.

(44) Zou, L.; He, Y.; Liu, Z.; Jia, H.; Zhu, J.; Zheng, J.; Wang, G.; Li, X.; Xiao, J.; Liu, J.; Zhang, J.-G.; Chen, G.; Wang, C. Unlocking the passivation nature of the cathode−air interfacial reactions in lithium ion batteries. *Nat. Commun.* **2020**, *11* (1), No. 3204.

(45) Magar, H. S.; Hassan, R. Y. A.; Mulchandani, A. Electrochemical Impedance Spectroscopy (EIS): Principles, Construction, and Biosensing Applications. *Sensors* **2021**, *21* (19), No. 6578, DOI: 10.3390/s21196578.

(46) Zhang, D.; Luo, Y.; Liu, J.; Dong, Y.; Xiang, C.; Zhao, C.; Shu, H.; Hou, J.; Wang, X.; Chen, M. $ZnFe_2O_4$−Ni_5P_4 Mott−Schottky Heterojunctions to Promote Kinetics for Advanced Li−S Batteries. *ACS Appl. Mater. Interfaces* **2022**, *14* (20), 23546−23557.

(47) Shen, Z.; Cao, L.; Rahn, C. D.; Wang, C.-Y. Least Squares Galvanostatic Intermittent Titration Technique (LS-GITT) for Accurate Solid Phase Diffusivity Measurement. *J. Electrochem. Soc.* **2013**, *160* (10), No. A1842, DOI: 10.1149/2.084310jes.

(48) Shaju, K. M.; Rao, G. V. S.; Chowdari, B. V. R. Influence of Li-Ion Kinetics in the Cathodic Performance of Layered Li-$(Ni_{1/3}Co_{1/3}Mn_{1/3})O_2$. *J. Electrochem. Soc.* **2004**, *151* (9), No. A1324, DOI: 10.1149/1.1775218.

(49) Simon, P.; Gogotsi, Y.; Dunn, B. Where Do Batteries End and Supercapacitors Begin? *Science* **2014**, *343* (6176), 1210−1211.

(50) Yang, H.; Qin, T.; Zhou, X.; Feng, Y.; Wang, Z.; Ge, X.; Yue, N.; Li, D.; Zhang, W.; Zheng, W. Boosting the kinetics of PF$_6$$^−$ into graphitic layers for the optimal cathode of dual-ion batteries: The rehearsal of pre-intercalating Li$^+$. *J. Energy Chem.* **2022**, *71*, 392−399.

(51) Brezesinski, T.; Wang, J.; Tolbert, S. H.; Dunn, B. Ordered mesoporous α-MoO_3 with iso-oriented nanocrystalline walls for thin-film pseudocapacitors. *Nat. Mater.* **2010**, *9* (2), 146−151.